Research Square

Preprints are preliminary reports that have not undergone peer review.
They should not be considered conclusive, used to inform clinical practice,
or referenced by the media as validated information.

Anthropogenic warming reshapes sea surface salinity away from simple pattern amplification

Yuxuan Lyu

yuxuan.lyu@utas.edu.au

university of Tasmania

Nathaniel Bindoff

University of Tasmania https://orcid.org/0000-0001-5662-9519

Sandeep Mohapatra

university of Tasmania

Saurabh Rathore

Indian Institute of Technology Delhi https://orcid.org/0000-0001-6677-6838

Helen Phillips

University of Tasmania https://orcid.org/0000-0002-2941-7577

Jiheun Lee

University of Tasmania

Article

Keywords:

Posted Date: November 17th, 2026

DOI: https://doi.org/10.21203/rs.3.rs-11738928/v1

License: This work is licensed under a Creative Commons Attribution 4.0 International License.
Read Full License

Additional Declarations: There is **NO** Competing Interest.

Anthropogenic warming reshapes sea surface salinity away from simple pattern amplification

Yuxuan Lyu[1,2], Nathaniel L. Bindoff[1,2,3], Sandeep Mohapatra[1,2], Saurabh Rathore[4], Helen E. Phillips[1,2,3] and Jiheun Lee[1]

1 Institute for Marine and Antarctic Studies, University of Tasmania, Hobart, TAS, Australia.

2 Australian Centre for Excellence in Antarctic Science, University of Tasmania, Hobart, TAS, Australia.

3 Australian Antarctic Program Partnership, Institute for Marine and Antarctic Studies, University of Tasmania, Hobart, TAS, Australia.

4 Centre for Atmospheric Sciences, Indian Institute of Technology Delhi, New Delhi, India.

Correspondence to Nathaniel L. Bindoff (N.Bindoff@utas.edu.au) or Yuxuan Lyu (yuxuan.lyu@utas.edu.au).

Abstract

Future sea surface salinity (SSS) changes are widely expected to follow pattern amplification (PA), scaling directly with historical hydrological patterns. Here we show, using 13 CMIP6 models, that projected SSS changes are instead better captured by warming-dependent patterns. SSS signals emerge from internal variability at lower warming levels and over larger ocean areas than evaporation minus precipitation (E-P) signals, while the amplitudes of both responses increase approximately linearly across 1-3°C of warming. At equivalent warming levels, SSS and E-P signal-to-noise patterns are highly consistent across emission pathways, with median spatial correlations of 0.89–0.98. At 3°C under SSP5-8.5, multi-model mean SSS changes differ substantially from PA expectations over 59.4% of the ocean, including 22.6% with opposite signs. At least 10 of the 13 models agree on reversals relative to PA over 6.2% of the ocean for SSS and 11.0% for E-P. Regional salinity budgets reveal that surface freshwater forcing is the primary driver of tropical SSS reversals, whereas horizontal advection promotes freshening in parts of the subtropical Pacific and North Atlantic. These warming-dependent patterns move beyond the PA paradigm by scaling future salinity changes with global warming, showing how historical SSS patterns break down under continued warming.

Main Text

Sea surface salinity (SSS) records the oceanic imprint of freshwater exchange and provides a widely used indicator of change in the global water cycle[1–3]. Observed and simulated changes often amplify the mean patterns of salinity and evaporation minus precipitation (E-P), consistent with an intensifying atmospheric water cycle[4–8]. For salinity, this pattern amplification (PA) is commonly described as "salty gets saltier, fresh gets fresher". However, regional SSS changes do not consistently follow PA under continued warming because ocean processes can modify the response to changing freshwater forcing[9–11]. Observations and climate model simulations show that freshening in precipitation-dominated regions is more robust than salinification in evaporation-dominated regions[12]. Recent observations also reveal salinification in climatologically fresh Southern Ocean waters around 40-50°S, linked to the poleward expansion of subtropical gyres[13].

Systematically characterizing the SSS response to global warming from available observations and reanalyses remains challenging because the anthropogenically forced signal of change in SSS (hereafter, the forced signal) is often obscured by internal climate variability[14]. Time of emergence (ToE) diagnostics identify when and where this forced signal persistently exceeds background internal variability[15]. Model-based studies have identified early emergence in surface salinity in parts of the polar oceans and the subtropical North Atlantic[16], as well as emerging anthropogenic changes in the ocean interior[17,18]. However, it remains unclear how future global SSS patterns evolve with warming across emissions pathways, how these changes correspond to those in E-P, and whether PA continues to describe regional change.

To identify global patterns of future SSS change, we analyze historical, pre-industrial control (piControl) and ScenarioMIP simulations from 13 models of the sixth phase of the Coupled Model Intercomparison Project (CMIP6)[19,20]. Comparing SSS and E-P signal-to-noise patterns at common global warming levels[21] allows us to assess spatial differences across emissions pathways (Methods). We also quantify how projected changes differ from PA expectations derived from their historical patterns and use regional mixed-layer salinity budgets to examine the contributions of surface freshwater forcing and ocean redistribution to regional freshening and salinification. These analyses connect the emergence of SSS changes and their consistency across emissions pathways with regional salinity processes, providing a new perspective for interpreting future SSS change beyond PA.

Emergence of anthropogenic fingerprints in SSS and E-P

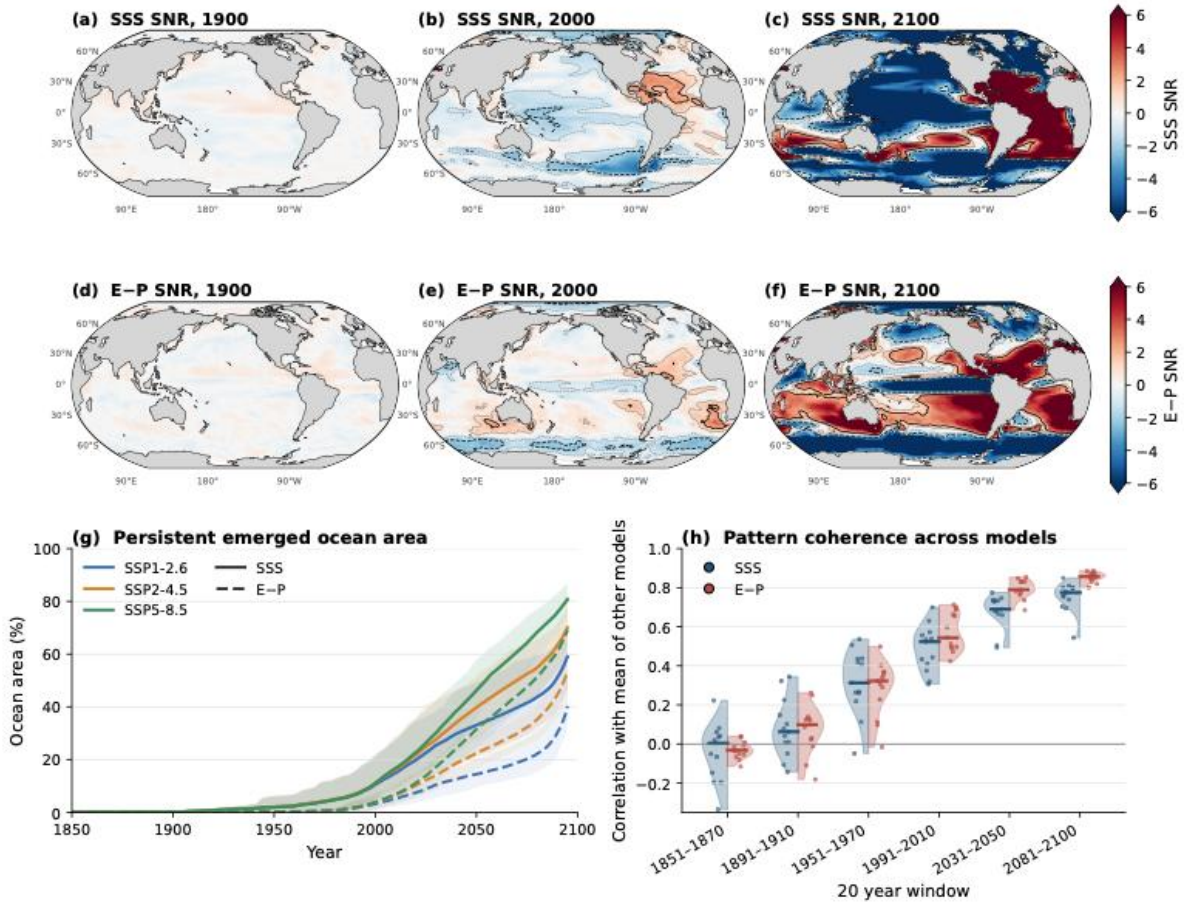


Fig. 1 | Emergence of anthropogenic SSS and E-P fingerprints. a-c, Multi-model mean (MMM) signed signal-to-noise ratio (SNR) of SSS under historical and SSP5-8.5 forcing for 1891-1910, 1991-2010 and 2081-2100, labelled 1900, 2000 and 2100, respectively. **d-f**, Corresponding MMM E-P maps. Positive (negative) values denote salinification (freshening) for SSS and increased net evaporation (precipitation) for E-P. Black contours mark SNR = ±2, the threshold used to diagnose emergence; grey contours mark SNR = ±1 for context. Solid and dashed contours indicate positive and negative values, respectively. **g**, Percentage of ocean area with persistent emergence under SSP1-2.6, SSP2-4.5 and SSP5-8.5, shown through 2095. Persistent emergence is evaluated from annual SNR series using $|SNR| \geq 2$ (Methods). Solid curves show SSS and dashed curves show E-P; curves and shading indicate the MMM and 10^{th}-90^{th} percentile range across 13 models, respectively. **h**, Evolution of inter-model pattern coherence along the combined historical and SSP5-8.5 trajectory. For each displayed 20-year window, points show the area-weighted spatial correlation between each model's SNR pattern and the mean pattern of the other 12 models. Half-violins show the distributions of the 13 model-specific correlations for SSS (left) and E-P (right), and horizontal bars mark the medians.

We diagnose emergence where the signal-to-noise ratio (SNR) satisfies $|SNR| \geq 2$, with noise estimated from pre-industrial control (piControl) simulations[22] (Methods). Along the combined historical and SSP5-8.5 trajectory (1850-2100), initially weak SSS and E-P signals develop into coherent basin-scale patterns (Fig. 1a-f). By 2095, freshening dominates the tropical Pacific, Indian Ocean, subpolar North Atlantic and much of the Southern Ocean, while salinification is strongest in the tropical and subtropical Atlantic (Fig. 1c). E-P shows increasing net precipitation in tropical and high-latitude sectors and stronger net evaporation across the subtropics (Fig. 1f), consistent with atmospheric water-cycle intensification under anthropogenic warming[4].

As the forced SSS and E-P signals strengthen after the late twentieth century, emergence expands across the ocean for both variables, with larger emerged areas under higher-emission pathways (Fig. 1g). By 2095, the MMM emerged fractions for SSS and E-P reach 59.0% and 40.3% under SSP1-2.6, 70.0% and 53.6% under SSP2-4.5, and 80.8% and 69.2% under SSP5-8.5, respectively. The broader emergence of SSS reflects greater detectability relative to its own internal variability. The inter-model spread in emerged area is also smaller under SSP5-8.5 than under SSP1-2.6, with the 10^{th}-90^{th} percentile ranges narrowing from 47.7-70.8% to 74.5-86.9% for SSS and from 33.4-50.0% to 63.3-74.7% for E-P (Fig. 1g; Supplementary Fig. 1). Spatial agreement among models also strengthens along the historical-SSP5-8.5 trajectory (Fig. 1h). For each 20-year window, we calculate the area-weighted spatial correlation between each model's SNR pattern and the mean SNR pattern of the remaining 12 models. By 2081-2100, the median of these 13 correlations reaches 0.77 for SSS and 0.86 for E-P. Despite substantial differences in internal variability among models[23] (Supplementary Fig. 2), the increasing agreement in their SNR patterns is consistent with a shared forced signal strengthening relative to internal variability[24].

Global warming level is a pathway-independent indicator of future change in Earth's hydrological cycle

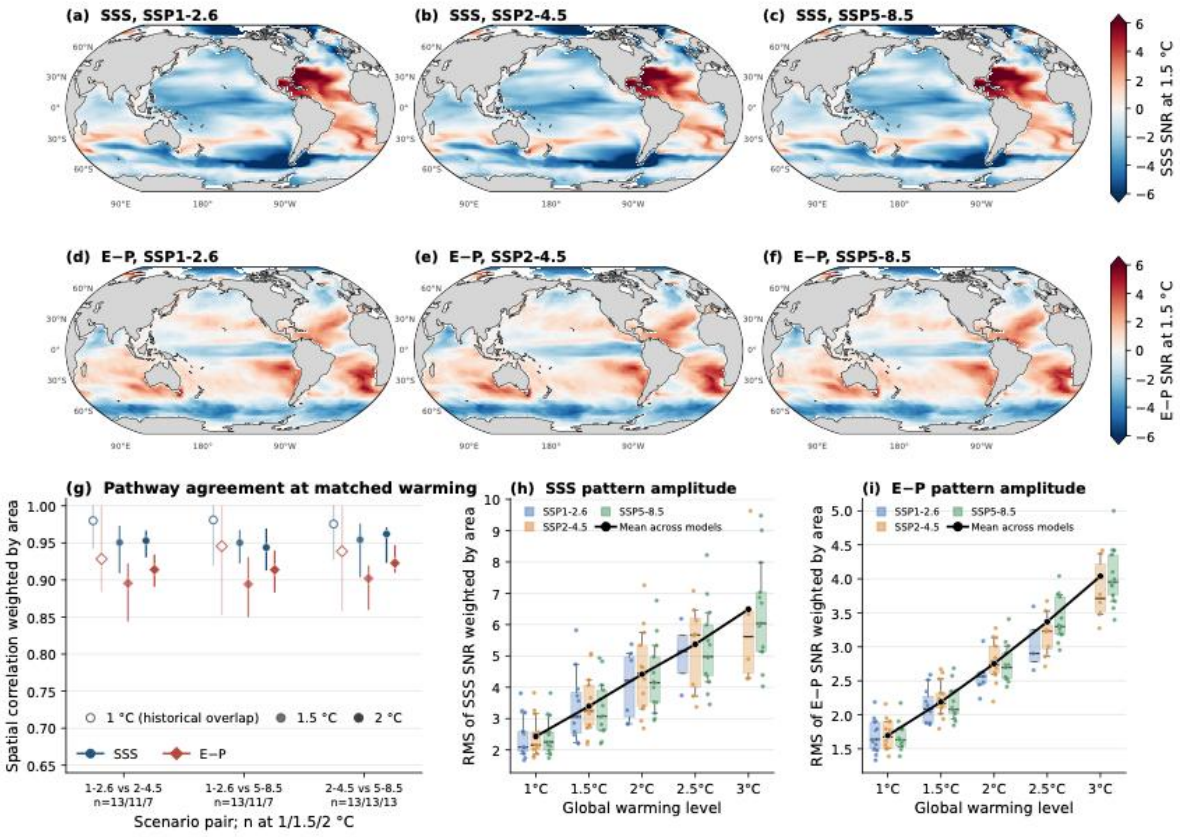


Fig. 2 | Warming level organizes SSS and E−P fingerprints across pathways. a-c, Multi-model mean signal-to-noise ratio of sea surface salinity at 1.5 °C under SSP1-2.6, SSP2-4.5 and SSP5-8.5. d-f, Corresponding E-P SNR patterns. Panels **a-f** use the same 11 models with available estimates for both variables at 1.5 °C under all three pathways. **g**, Spatial agreement between pathways at the same warming levels. Area-weighted correlations between pathway-specific SNR patterns are calculated within each model. Symbols show the median across models, and bars indicate the 10^{th}-90^{th} percentile range. Open symbols at 1 °C identify comparisons in which some pathway windows share historical years. Sample sizes beneath each pathway pair refer to 1, 1.5 and 2 °C, respectively. **h, i**, Area-weighted RMS amplitude of SSS and E-P SNR. Points show individual models. Boxes span the interquartile range, center lines mark medians and whiskers the 10^{th}-90^{th} percentile range. Black lines connect MMM after pathways are first averaged within each model.

The increasing coherence of the SNR fingerprints across models raises the question of whether their spatial patterns also agree across emissions pathways at the same warming level. At the Paris Agreement's 1.5°C warming target[25], both SSS and E-P show consistent basin-scale patterns across the three emission pathways (Fig. 2a-f). Comparisons between emission pathways within each model give median area-weighted spatial correlations of approximately 0.95 for SSS and 0.89-0.90 for E-P across pathway pairs (n = 11-13; Fig. 2g). This agreement extends to 2°C warming, with corresponding correlations of 0.94-0.96 and 0.91-0.92, respectively (n = 7-13). The 1°C estimates are also high, at 0.98 for SSS and 0.93-0.95 for E-P (n = 13). However, some of these 20-year windows include overlapping data from the same historical simulation before 2015, so the corresponding pathway comparisons are not fully independent (Supplementary Table 2). These comparisons show that the large-scale SNR patterns are very similar across emissions pathways when evaluated at a common warming level.

The strength of the response increases with warming. The area-weighted root mean square (RMS) of SNR increases for both variables (Fig. 2h, i), indicating that their forced signals strengthen relative to internal variability. The underlying SSS and E-P change fields also show an approximately linear increase in spatial RMS amplitude over 1-3°C warming. Linear fits within individual models give mean slopes of 0.121 PSU K^{-1} for SSS (95% confidence interval, 0.095-0.144) and 0.172 mm day^{-1} K^{-1} for E-P (0.154-0.192; Supplementary Fig. 3a, b). Averaged across models, these fits explain 89% of the variance in SSS response amplitude and 95% in E-P response amplitude (Supplementary Data 1), showing that warming level provides a useful basis for comparing the magnitude of their responses across pathways.

To examine whether scaling with warming also captures spatial structure, we reconstruct each model's SSS and E-P changes using warming-dependent relationships estimated from the remaining models (Methods). Across the available models, pathways and warming levels, the median spatial correlation between reconstructed and simulated change fields is 0.66, with a 10^{th}-90^{th} percentile range of 0.42-0.76 (Supplementary Fig. 3e, f). The reconstruction captures common basin-scale features but does not reproduce all regional detail, consistent with the broader limitations of pattern scaling[26]. For SSS, ocean transport and mixed-layer processes also shape the regional response to freshwater forcing[1,8,10], highlighting the need to examine regional changes alongside the large-scale relationship with warming.

Regional changes depart from pattern amplification

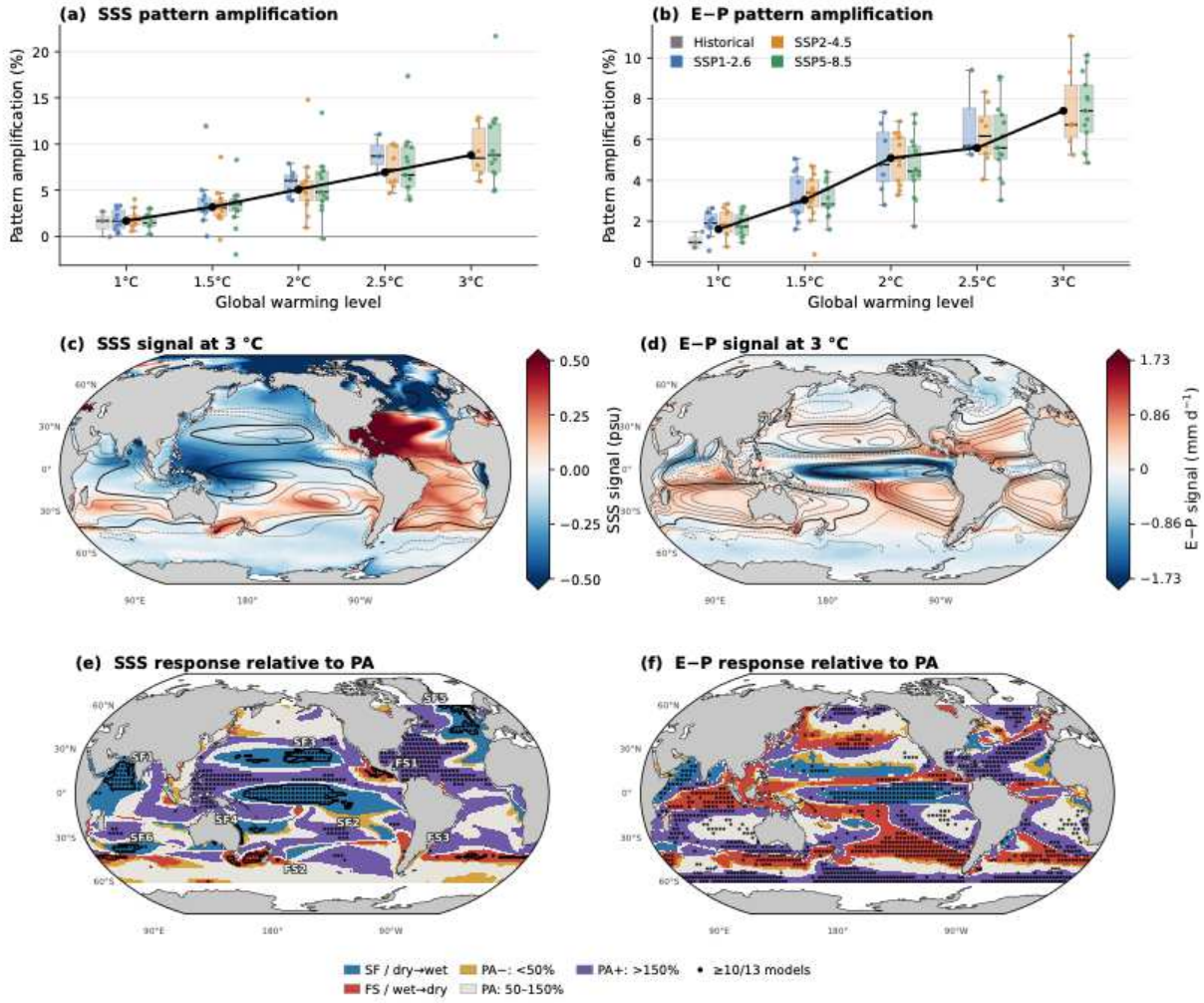


Fig. 3 | Pattern amplification strengthens with warming, while regional changes depart from its expectations. a, SSS PA and b, E-P PA as a function of warming level. For every model and pathway, the 20-year average change relative to 1950-2014 is regressed onto the fixed 1950-2014 climatological anomaly pattern. The regression coefficient defines accumulated PA and is expressed as a percentage. For example, a 5% SSS PA means that the fitted response strengthens historical salinity contrasts by 5%. Points show individual estimates and boxplots summarize each experiment. Grey points are three CMIP6 historical windows that reach 1 °C before the scenario period. Black lines connect the medians across models after pathways are first averaged within each model. **c, d,** Multi-model mean SSS and E-P changes at 3 °C under SSP5-8.5. Contours show the 1950-2014 climatological anomaly patterns, with solid and dashed lines indicating positive and negative anomalies, respectively. **e, f,** Local response relative to the PA expectation. In **e**, blue denotes freshening in climatologically salty waters (SF, salty→fresh), and red denotes salinification in climatologically fresh waters (FS, fresh→salty). In **f**, blue denotes decreasing E-P in climatologically drier regions (dry→wet), and red denotes increasing E-P in climatologically wetter regions (wet→dry). Stippling marks agreement among at least 10 of 13 models. Labels in **e** identify the six SF and three FS regions analyzed in Fig. 4.

The large-scale SSS and E-P responses to global warming show clear spatial differences from their respective historical climatological patterns (Fig. 3c, d). We therefore quantify PA across CMIP6 models and warming levels to examine where the projected changes strengthen, weaken or reverse these historical contrasts (Fig. 3; Methods). Multi-model mean SSS PA increases approximately linearly with warming, indicating that the fitted PA response strengthens historical salinity contrasts by 1.71% at 1°C and 10.00% at 3°C. The 10th-90th percentile ranges are 0.41-3.06% and 5.72-12.68%, respectively (Fig. 3a). Mean E-P PA also strengthens over this interval, rising from 1.67% (0.79-2.52%) to 7.54% (5.35-9.98%; Fig. 3b). Linear fits over 1-3°C give model-mean increases of 4.24 % K^{-1} for SSS PA and 2.95 % K^{-1} for E-P PA (Methods), with SSS PA also showing a wider inter-model spread at higher warming levels. Earlier salinity-based studies inferred historical water-cycle intensification of 8 ± 5% K^{-1} over 1950-2000 from surface salinity observations and CMIP3 simulations[6] and 3.0 ± 1.6% K^{-1} over 1950-2010 from full-depth salinity observations using a salt-conservation framework[27]. These estimates describe historical water-cycle intensification inferred from salinity, whereas our slopes quantify the warming sensitivity of SSS and E-P PA.

This overall strengthening nevertheless conceals substantial regional departures from PA expectations in both the direction and magnitude of change. At 3°C under SSP5-8.5, multi-model mean SSS changes oppose the PA expectation over 22.6% of the ocean (Fig. 3c, e). Freshening in climatologically salty waters accounts for 18.0% of the ocean, while salinification in climatologically fresh waters accounts for 4.6%. We refer to these reversals as salty-to-fresher (SF) and fresh-to-saltier (FS), respectively. Even where changes follow the PA direction, their magnitudes often differ from the expectation. We distinguish weakened PA (PA-, below 50% of the PA expectation), PA-consistent responses (PA, 50-150%) and enhanced PA (PA+, above 150%; Methods). Weakened responses cover 5.4% of the ocean for SSS and 6.1% for E-P, whereas enhanced responses cover 31.5% and 31.0%, respectively (Fig. 3e, f; Supplementary Fig. 5c).

Agreement among at least 10 of the 13 models supports SSS reversals over 6.2% of the ocean. E-P reversals are more extensive, covering 30.0% of the ocean, with at least 10 models agreeing over 11.0% (Fig. 3f; Supplementary Fig. 5a-c). As a robustness test, relaxing this criterion to at least nine models increases the reversal areas to 9.7% for SSS and 15.0% for E-P, whereas requiring agreement among at least eleven models reduces them to 3.2% and 7.5%, respectively (Supplementary Fig. 5d).

SSS reversals cluster along tropical and subtropical salinity gradients and near ocean fronts (Fig. 3e). This distribution is consistent with ocean transport modifying the regional imprint of freshwater

forcing[8,10,28]. E-P reversals form broader regions around subtropical evaporation zones and tropical rainfall maxima (Fig. 3f), where shifts in the location or extent of these features can produce local changes opposite to PA. Such changes could reflect the poleward expansion of subtropical dry zones associated with Hadley circulation widening[29,30] and the equatorward contraction of the tropical rain belt[31]. The partial overlap between SSS and E-P reversals highlights the need to distinguish the contributions of surface freshwater forcing and ocean redistribution. We therefore examine mixed-layer salinity budgets in six SF and three FS regions with strong model agreement to assess how these processes contribute to the SSS reversals (Fig. 3e; Supplementary Table 4).

Mechanisms of regional salinity reversals

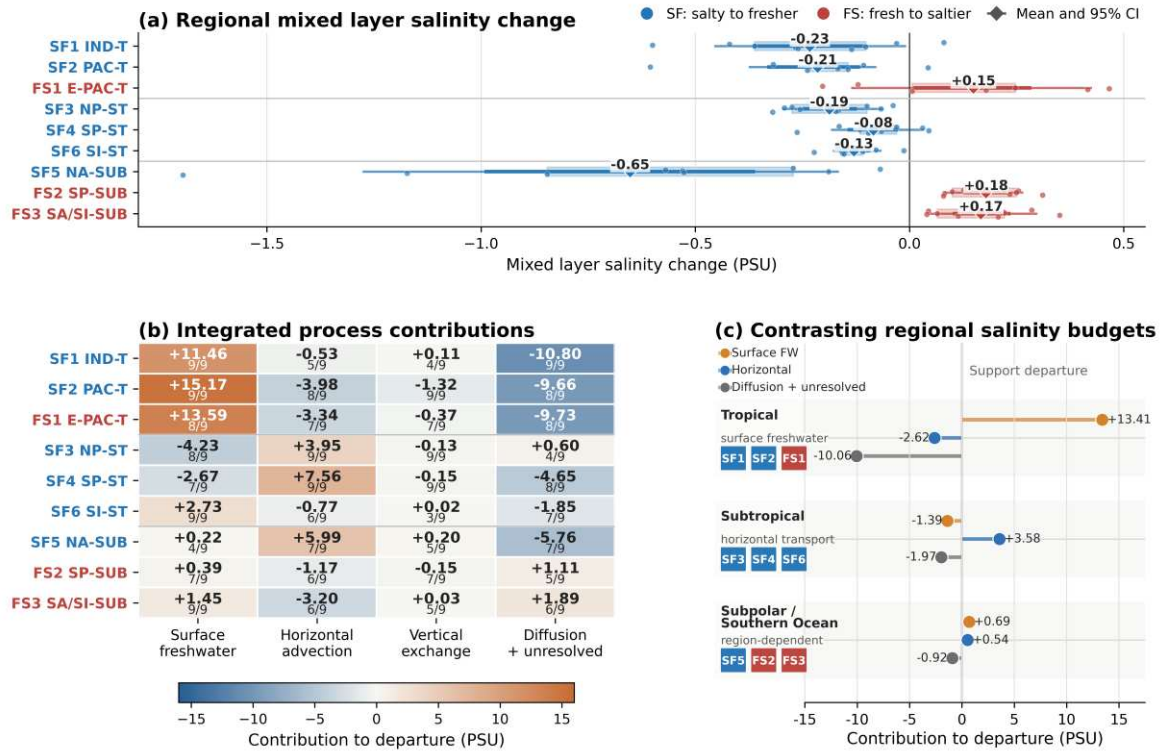


Fig. 4 | Mixed-layer contributions to regional salinity reversals relative to pattern amplification. a, Regional mixed layer salinity change between the 1950-2014 mean and each model's centered 20-year SSP5-8.5 window at 3 °C. Points show nine models. Diamonds show the multi-model mean and thick bars its bootstrap 95% confidence interval, while shaded boxes and thin bars indicate the interquartile and 10th-90th percentile ranges across models, respectively. **b, Accumulated mixed-layer** salinity budget contributions for the same regions. Monthly terms are referenced to their 1950-2014 calendar month climatology and integrated from January 1950. Values are aligned so that positive contributions support SF freshening or FS salinification, whereas negative contributions oppose these changes. Cells show the nine-model mean integrated contribution in PSU, with smaller numbers indicating the number of models with the same sign as the mean. Diffusion plus unresolved processes combine horizontal and vertical diffusion with the offline residual. **c,** Process contributions grouped across tropical, subtropical and subpolar/Southern Ocean regions with bars showing the multi-model mean averaged over the regions in each setting.

At 3°C warming under SSP5-8.5, mean mixed-layer freshening relative to 1950-2014 ranges from 0.08 PSU in the subtropical South Pacific (SF4) to 0.65 PSU in the North Atlantic (SF5), whereas the three FS regions salinify by 0.15-0.18 PSU. At least seven of the nine budget models reproduce the corresponding freshening or salinification in each region (Fig. 4a).

Surface freshwater forcing provides the dominant resolved contribution to salinity reversals in the three tropical regions (Fig. 4b, c). All nine models show surface-driven freshening in the tropical Indian Ocean (SF1) and tropical Pacific (SF2), with mean accumulated contributions of 11.46 and 15.17 PSU, respectively. In the eastern tropical Pacific (FS1), surface forcing promotes salinification in eight models, contributing 13.59 PSU on average. These large surface contributions are mostly offset by the combined diffusion and unresolved term, while horizontal advection and vertical exchange also oppose freshening in SF2 and salinification in FS1. Outside the tropics, surface forcing consistently promotes freshening in the subtropical South Indian Ocean (SF6), with agreement among all nine models and a mean accumulated contribution of 2.73 PSU.

Horizontal advection provides the main resolved contribution to freshening in the subtropical North Pacific (SF3), subtropical South Pacific (SF4) and North Atlantic (SF5; Fig. 4b). In SF3 and SF4, mean accumulated freshening from horizontal advection is 3.95 and 7.56 PSU, respectively, with all nine models agreeing on the direction. Surface forcing and vertical exchange oppose this advective freshening in both regions, while the combined diffusion and unresolved term also promotes salinification in the South Pacific. This opposition between advection and surface forcing is consistent with earlier budget studies showing that ocean transport redistributes freshwater and modifies the salinity response to surface fluxes[1,8,10]. In the North Atlantic, advection contributes 5.99 PSU towards freshening, with agreement among seven models, but much of this contribution is offset by the combined diffusion and unresolved term. Surface forcing and vertical exchange are smaller in the ensemble mean, and models disagree on whether they promote freshening or salinification (Supplementary Table 5).

A common resolved explanation for net salinification remains unclear in the South Pacific (FS2) and South Atlantic-Indian Ocean sector (FS3), where the combined diffusion and unresolved term promotes salinification in the ensemble mean (Fig. 4b). In the South Pacific, surface forcing promotes salinification in seven models, but differences in the sign and magnitude of the process contributions prevent a clear attribution to a common resolved driver (Supplementary Table 5). In the South Atlantic-Indian Ocean sector, surface freshwater forcing promotes salinification in all nine models,

with a mean accumulated contribution of 1.45 PSU. This is opposed by 3.20 PSU of advective freshening, while the combined diffusion and unresolved term contributes a further 1.89 PSU towards salinification. Surface forcing therefore makes a consistent contribution in this region, but explaining the net change also requires contributions that cannot be fully attributed to resolved processes.

Across the 81 model-region budgets, the ratio of the absolute offline residual to the largest resolved contribution has a median of 0.67 and a 90th percentile of 1.16, using surface forcing, horizontal advection, vertical exchange and combined horizontal and vertical diffusion for the comparison (Methods; Supplementary Data 3). The diffusion estimate and offline residual are strongly anticorrelated ($r = -0.92$; Supplementary Fig. 6c), partly because the residual is defined by subtracting the diffusion estimate (Methods). Their sum is reported as the combined diffusion and unresolved term, whose relative importance varies among models and regions (Supplementary Fig. 6d). Although this term does not isolate physical mixing, the principal surface-forcing and advective contributions retain their directions in ensemble means, medians and leave-one-model-out tests (Methods; Supplementary Fig. 6a, b; Supplementary Table 5).

Discussion

Our analysis identifies warming-dependent patterns of future SSS and E-P change whose large-scale structures remain highly consistent across emissions pathways at the same warming levels. Although PA also strengthens with global warming, it does not describe most of the regional changes within these future patterns. At 3°C warming, MMM SSS changes depart from the PA expectation across 59.4% of the ocean, including sign reversals across 22.6% of the ocean. Our mixed-layer budgets identify surface freshwater forcing as the main resolved contribution to tropical salinity reversals relative to PA, while horizontal advection consistently promotes freshening in the subtropical Pacific and North Atlantic.

Our emergence results suggest that SSS can reveal anthropogenic influence earlier and over a wider ocean area than E-P (Fig. 1g). Based on previous studies of anthropogenic influence on ocean salinity[32–35] and time of emergence[15–17], our results connect the emergence of these signals with their evolution for different warming levels. We show that at the same warming levels, their SNR patterns are highly consistent across emissions pathways, with median correlations of 0.94-0.98 for SSS and 0.89-0.95 for E-P (Fig. 2g). For each 1°C of global warming, the area-weighted RMS amplitudes of SSS and E-P changes increase on average by 0.121 PSU and 0.172 mm day^{-1}, respectively (Supplementary Fig. 3a, b). These findings support the use of global warming levels to compare

projections across emissions pathways[36,37]. Warming-scaled reconstructions capture the broad spatial patterns of simulated SSS and E-P change (median r = 0.66; Supplementary Fig. 3e, f).

SSS and E-P PA strengthen with warming, consistent with earlier evidence of an intensifying global water-cycle[6,27,38–41]. Regional reversals nevertheless remain robust across models: at 3°C warming, at least 10 of the 13 models agree on SSS trend reversals over 6.2% of the ocean (Fig. 3e; Supplementary Fig. 5). These robust reversals are more extensive in the Northern Hemisphere, which accounts for 60.8% of their total area. In the multi-model mean, freshening in climatologically salty waters covers 18.0% of the ocean, compared with 4.6% for salinification in climatologically fresh waters. This predominance of freshening in salty waters is consistent with previous findings that the "salty gets saltier" response is less robust than the "fresh gets fresher" response[12]. E-P trend reversals cover 30.0% of the ocean and cluster near subtropical evaporation zones and tropical rainfall bands (Fig. 3f). Shifts in these evaporation and rainfall zones can produce local E-P changes opposite to the PA expectation even as the large-scale water cycle intensifies[29–31]. The partial overlap between SSS and E-P trend reversals is consistent with a contribution from surface freshwater forcing, while their regional differences point to an additional role for ocean transport and mixed-layer processes[8,10,11,42]. Together, these results show that PA alone cannot fully describe future SSS change, while CMIP6 projections reveal how SSS and E-P patterns evolve with warming.

Surface freshwater forcing promotes freshening in the tropical Indian Ocean (SF1) and tropical Pacific (SF2) and salinification in the eastern tropical Pacific (FS1; Fig. 4). Its importance is consistent with ocean-model sensitivity experiments and CMIP6 projections linking tropical salinity changes to changes in precipitation and evaporation, while showing that ocean circulation modifies their regional distribution[43,44]. Surface forcing also consistently promotes freshening in the subtropical South Indian Ocean (SF6), indicating that its contribution to regional reversals is not confined to the tropics. These regions show that salinity changes opposite to the PA expectation can remain consistent with the direction of the local surface freshwater contribution. In the subtropical North and South Pacific (SF3 and SF4), by contrast, horizontal advection promotes freshening while surface forcing promotes salinification, consistent with earlier budget analyses showing that ocean redistribution limits salinity accumulation in evaporation-dominated waters[8,10]. Horizontal advection also provides the clearest resolved freshening contribution in the North Atlantic (SF5), where models disagree on the direction of the smaller surface contribution (Supplementary Table 5). This advective freshening is physically consistent with reduced northward transport of saline subtropical waters

associated with projected AMOC weakening[45]. The role of redistribution in these regions complements observational evidence that ocean warming and freshwater transport reshape salinity patterns beyond the imprint of local surface fluxes[46,47]. Net salinification in the South Pacific (FS2) and South Atlantic-Indian Ocean sector (FS3) remains less clearly explained because the budgets contain substantial combined diffusion and unresolved contributions and differ among models (Supplementary Fig. 6; Supplementary Table 5).

By linking the emergence and warming dependence of SSS and E-P patterns with regional salinity budgets, our study provides a new method for interpreting recent and future surface salinity change as a function of global warming levels. It enables direct comparisons of projections across emissions pathways at the same warming level, while regional budgets assess how surface freshwater forcing and ocean redistribution shape projected freshening and salinification. This method could also be extended to investigate how changes in mean salinity and circulation interact with internal climate variability to shape salinity extremes[45,48,49]. Together, these warming-dependent patterns and regional budgets provide a basis for evaluating future salinity observations and assessing global and regional salinity responses in climate models, while offering a more complete description of future salinity change than historical PA alone.

Methods

CMIP6 simulations, variables and observational products

We use historical, piControl and ScenarioMIP simulations from 13 CMIP6 models: ACCESS-CM2, ACCESS-ESM1-5, BCC-CSM2-MR, CESM2, CMCC-CM2-SR5, CanESM5, EC-Earth3, FGOALS-g3, GFDL-ESM4, IPSL-CM6A-LR, MIROC6, MPI-ESM1-2-LR and MRI-ESM2-0[19,20]. We analyze one realization from each model under SSP1-2.6, SSP2-4.5 and SSP5-8.5, with model-specific variant labels listed in Supplementary Table 1. The primary variables are SSS, evaporation and precipitation, with positive evaporation minus precipitation (E-P) denoting net evaporation. Near-surface air temperature is used to determine model-specific global warming levels.

The SSS and E-P fields used in Figs. 1-3 are remapped to a common 1° grid before the global analyses. Mixed-layer salinity budgets are calculated separately for nine models using monthly three-dimensional salinity, potential temperature, horizontal velocity and surface freshwater mass flux. Budget terms are diagnosed on the native model grids and then mapped to the fixed stippled cells within the nine SF and FS regions identified in Fig. 3e. Model availability is listed in Supplementary Table 1.

Observational and reanalysis products are used to benchmark the historical mean SSS and E-P fields represented by CMIP6. We use EN4[50], IAP[51] , ORAS5[52] datasets for SSS and ERA5[53] for E-P over 1979-2014. Supplementary Fig. 4 compares the observed and simulated mean states, and product details are listed in Supplementary Table 3.

Signal, noise and persistent emergence

For each model, linear drift is estimated from the final 300 years of the corresponding piControl simulation and removed from the forced and control fields. Forced anomalies are referenced to the drift-corrected mean over the first 100 years of piControl following the historical branch point. The forced and piControl anomalies are smoothed using a centered 10-year running mean.

The internal variability, hereafter noise, is the standard deviation of the smoothed, drift-corrected piControl anomaly series over the final 300 years at each grid point. For the warming level analysis, the processed signal and signal-to-noise (SNR) fields are averaged over the model-specific 20-year window associated with each warming level. For model i, variable X, grid cell x and time t, the SNR is:

$$SNR_i^X(x,t) = \frac{\Delta X_i(x,t)}{\sigma_i^X(x)} \quad (1)$$

Where X is SSS or E-P. $\Delta X_i(x,t)$ denotes the estimated forced signal, and $\sigma_i^X(x)$ is the local standard deviation of the equivalently processed piControl anomaly series. Negative SNR denotes freshening for SSS and increasing net precipitation for E-P. Positive SNR denotes salinification for SSS and increasing net evaporation for E-P. A grid cell is defined as emerged when |SNR| ≥ 2.

Persistent emergence begins in the first year from which the smoothed annual SNR satisfies |SNR| ≥ 2 for the remainder of the available record[15,17,22,54]. The persistent emerged fraction is

$$f_{persistent}(t) = 100 \times \frac{\Sigma_x w_x I[t_{ToE}(x) \leq t]}{\Sigma_x w_x} \quad (2)$$

where $f_{persistent}(t)$ is the emerged ocean fraction at time t. w_x is grid cell area, $t_{ToE}(x)$ is the persistent emergence time at grid cell x, and I is an indicator that equals one when the condition is met and zero otherwise. Figure 1g reports the model mean and 10th-90th percentile range. Supplementary Fig. 1 shows model spread and internal noise for the primary |SNR| ≥ 2 threshold.

Global warming levels and pathway agreement

Global warming is calculated from each model's annual global mean near-surface air temperature relative to 1850-1900. The historical and scenario simulations are joined at the 2014-2015 boundary to form a continuous time series, which is then smoothed using a centered 20-year running mean. For each model and pathway, we identify the first year in which the smoothed warming reaches 1, 1.5, 2, 2.5 or 3°C. The corresponding 20-year analysis window extends from nine years before to ten years after that year. Some 1°C windows fall partly or wholly within the historical experiment, including the three CMIP6 historical estimates shown in Fig. 3a, b. Higher warming levels use the scenario simulations where available. Exact windows are listed in Supplementary Table 2.

Pathway agreement and the performance of leave-one-model-out reconstructions are assessed using area-weighted spatial correlations over the common ocean mask:

$$r_{ab} = \frac{cov_w(A,B)}{\sqrt{var_w(A)\, var_w(B)}} \quad (3)$$

Here r_{ab} is the area-weighted spatial correlation between maps A and B. Weighted covariance and variance are denoted by cov_w and var_w. Pathway correlations are calculated within each model at

warming levels reached under both pathways. For Fig. 2h, i, pathways are averaged within each model before taking the multi-model mean (MMM).

SSS and E-P change scaled by warming

To estimate spatial responses per degree of global warming, we fit the following linear relationship at each grid cell separately for each model:

$$\Delta X_i(x,T) = \alpha_i^X(x) + \beta_i^X(x)T + \varepsilon_i(x,T) \quad (4)$$

where T is global warming level. $\Delta X_i(x,T)$ is the 20-year mean SSS or E-P anomaly at T, $\alpha_i^X(x)$ is the fitted intercept, $\beta_i^X(x)$ is the local change per Kelvin and $\varepsilon_i(x,T)$ represents residual departures from the fitted linear relationship. For each model, we fit the regression using the available warming-level samples from SSP1-2.6, SSP2-4.5 and SSP5-8.5. The multi-model mean response per kelvin is obtained by averaging the model-specific slopes with equal weight. For leave-one-model-out reconstruction, the coefficients are averaged over the remaining models and used to reconstruct the omitted model's response.

The area-weighted root mean square (RMS) change amplitude is

$$A_i^X(T) = \sqrt{\frac{\Sigma_x\, w_x[\Delta X_i(x,T)]^2}{\Sigma_x\, w_x}} \quad (5)$$

where $A_i^X(T)$ is the amplitude of change for model i and variable X at warming level T. The weight w_x is grid cell area, and the sums are over all ocean grid cells in the analysis mask. For each model, we fit a linear relationship with an intercept between this amplitude and global warming, using the available warming-level samples from SSP1-2.6, SSP2-4.5 and SSP5-8.5. The reported coefficients, 0.121 PSU K^{-1} for SSS and 0.172 mm day^{-1} K^{-1} for E-P, are the equal-weight means of the model-specific slopes. These slopes describe the growth of the spatial RMS amplitude per kelvin of warming, rather than a uniform change at every grid cell. Uncertainty in the mean slope is estimated by resampling the model-level fitted slopes with replacement 5,000 times and taking the 2.5th and 97.5th percentiles of the resampled means. These results are shown in Supplementary Fig. 3a, b, with the fitted coefficients provided in Supplementary Data 1. The spatial responses and leave-one-model-out reconstruction performance are shown in Supplementary Fig. 3c-f.

Pattern amplification at fixed warming levels

PA of SSS and E-P is diagnosed by projecting the warming-level change onto the corresponding fixed 1950-2014 climatological anomaly pattern over the Atlantic, Pacific and Indian oceans between 60° S and 60° N. For each model, the historical climatological anomaly and the 20-year mean change relative to 1950-2014 are first averaged zonally within each basin, after which the valid basin-latitude samples are combined in an ordinary least-squares regression with an intercept and equal sample weights, giving PA for model $i\ at$ warming level T as:

$$\mathrm{PA_i}(T) = 100 \times \frac{\mathrm{cov}\left(\overline{X'_{\mathrm{hist},i}}, \overline{\Delta X}_i(T)\right)}{\mathrm{var}\left(\overline{X'_{\mathrm{hist},i}}\right)} \quad (6)$$

Here, $X'_{hist,i}$ is the fixed 1950-2014 climatological anomaly, and $\Delta X_i(T)$ is the 20-year mean change in SSS or E-P at warming level T, relative to 1950-2014. The terms cov and var denote the covariance and variance calculated with equal weights across the valid basin-latitude samples, and PA is expressed as a percentage.

At each warming level, available pathways are first averaged within each model. The mean and 10th-90th percentile range across models are reported in the text, while the black lines in Fig. 3a, b connect the model medians. To estimate the warming sensitivity of PA, the pathway-averaged values are fitted against warming level over 1-3°C using an ordinary least-squares regression with an intercept for each model. The resulting slopes are averaged with equal model weights and expressed in % K^{-1}. Individual model, pathway and warming-level PA estimates are provided in Supplementary Data 2.

Classes relative to PA

For Fig. 3e, f, we use the mean PA at 3 °C to scale the multi-model mean historical climatological anomaly pattern. This gives the change that would occur at each grid cell under uniform pattern amplification. We compare this with the simulated multi-model mean change to classify each grid cell. Opposite sign cells define SF and FS reversals, depending on whether salty climatological waters freshen or climatologically fresh waters become saltier. Same sign cells are classified as weakened, consistent or enhanced PA when the simulated change is less than 50%, within 50-150%, or greater than 150% of the PA expectation. Cells with near-zero PA expectations are classified only when they meet the sign-reversal criteria. Otherwise, they remain unclassified, sharing the PA-consistent background color in the maps but contributing only to the denominator of the class area fraction.

Stippling marks agreement among at least 10 of 13 models, and Supplementary Fig. 5 and Supplementary Table 4 give the agreement and region definitions.

Mixed layer salinity diagnostics

Figure 4 uses transient integrals of the mixed layer salinity budget in the nine SF and FS regions. The calculation uses nine CMIP6 models with monthly salinity, potential temperature, horizontal velocity and surface freshwater flux fields (Supplementary Table 1).

Each resolved monthly budget term is converted to an anomaly by subtracting its 1950-2014 monthly climatology and then accumulated from 1950. Figure 4 uses the 3 °C window mean of each accumulated term relative to 1950-2014. For the accumulated budget, the residual is the difference between the diagnosed salinity change and the summed resolved contributions.

Monthly mixed layer depth h is diagnosed from potential density using a 0.03 kg m^{-3} increase from 10 m, following de Boyer Montégut et al.[55]:

$$\sigma_0(z_{MLD}) - \sigma_0(10\,m) = 0.03\,kg\,m^{-3} \quad (7)$$

Here, σ_0 is potential density referenced to the surface, z_{MLD} is the depth satisfying the density criterion, and depth is positive downward. Mixed layer salinity is

$$S_{ML} = \frac{1}{h}\int_0^h S(z)\,dz \quad (8)$$

where S(z) is salinity at depth z, the subscript ML denotes the mixed layer mean, and h is the monthly mixed layer depth.

The monthly mixed layer salinity tendency is written as

$$\frac{\partial S_{ML}}{\partial t} = F_{sfc} + A_h + E_{vert} + D_h + D_v + R \quad (9)$$

The terms on the right are, in order, surface freshwater forcing, horizontal advection, vertical exchange, horizontal and vertical diffusion and the residual.

Surface freshwater forcing is calculated from wfo, which is positive into the ocean:

$$F_{sfc} = -\frac{S_{ML}\,wfo}{\rho_0 h} \quad (10)$$

where ρ0 is reference seawater density. Horizontal advection is

$$A_h = -u_{ML} \frac{\partial S_{ML}}{\partial x} - v_{ML} \frac{\partial S_{ML}}{\partial y} \quad (11)$$

where velocity is averaged over the mixed layer. Vertical exchange is the sum of vertical advection at the mixed layer base and entrainment across the moving mixed layer base:

$$E_{vert} = E_{vadv} + E_{ent} \quad (12)$$

$$E_{vadv} = -\frac{S_b - S_{ML}}{h} w_b \quad (13)$$

$$E_{ent} = \frac{S_b - S_{ML}}{h} \left(\frac{\partial h}{\partial t} + u_b \frac{\partial h}{\partial x} + v_b \frac{\partial h}{\partial y}\right) \quad (14)$$

Here, subscript b denotes values at the mixed layer base, and w_b is positive downward. Vertical velocity is diagnosed from horizontal volume transports using continuity on each model's grid, accounting for layer-volume changes and the surface freshwater boundary condition where applicable. Vertical advection and moving-boundary exchange are evaluated consistently with the model's vertical coordinate and reported together as vertical exchange in Fig. 4.

Horizontal and vertical diffusion are represented by fixed coefficients of 10^4 m^2 s^{-1} and 10^{-4} m^2 s^{-1}. These prescribed values are not native model mixing tendencies.

$$R = \frac{\partial S_{ML}}{\partial t} - (F_{sfc} + A_h + E_{vert} + D_h + D_v) \quad (15)$$

For Fig. 4, all terms are aligned so that positive values support SF freshening or FS salinification. Horizontal and vertical diffusion are combined with the residual as diffusion plus unresolved because they compensate strongly across model and region budgets (Supplementary Fig. 6c, d).

Figure 4 reports the nine model mean contributions. For the leave-one-model-out test, we omit each model in turn and recalculate the ensemble mean contribution from the remaining eight models. Supplementary Fig. 6 compares means, medians and model sign support, and Supplementary Table 5 gives bootstrap intervals, sign counts and leave-one-model-out ranges. The model, region and process budget integrals are provided in Supplementary Data 3.

Data availability

The CMIP6 model output used in this study is publicly available through the Earth System Grid Federation. We used historical, piControl and ScenarioMIP simulations under SSP1-2.6, SSP2-4.5 and SSP5-8.5. The observational and reanalysis products used for historical evaluation are publicly available from the Met Office Hadley Centre (EN4), the Institute of Atmospheric Physics ocean data archive (IAP), and the Copernicus Climate Data Store for ORAS5 and ERA5. The accompanying Supplementary_Data.xlsx workbook contains warming scaled response fits, warming level PA estimates and regional mixed layer budget integrals. Additional processed data supporting the findings are available from the corresponding author on request.

Code availability

The analysis and plotting code is available from the corresponding author on request.

Acknowledgements

Y.L. acknowledges support from the Institute for Marine and Antarctic Studies, the Australian Centre for Excellence in Antarctic Science and the Australian Antarctic Program Partnership, and a PhD scholarship from the China Scholarship Council through grant **202106330073**. The analysis used CMIP6 model output made available by the modelling centers participating in CMIP6 and the Earth System Grid Federation. Computational support was provided by the National Computational Infrastructure, Australia. NLB is funded by the Australian Research Council through grant **FL240100141.**

Author contributions

N.L.B. and Y.L. conceived the study. Y.L. performed the data analysis and wrote the first draft. All authors contributed to scientific discussions, interpretation of the results and revision of the manuscript.

References

1. Yu, L. A global relationship between the ocean water cycle and near-surface salinity. *J. Geophys. Res.* **116**, C10025 (2011).
2. Durack, P. Ocean Salinity and the Global Water Cycle. *oceanog* **28**, 20–31 (2015).
3. Yu, L., Josey, S. A., Bingham, F. M. & Lee, T. Intensification of the global water cycle and evidence from ocean salinity: a synthesis review. *Ann. N.Y. Acad. Sci.* **1472**, 76–94 (2020).
4. Held, I. M. & Soden, B. J. Robust Responses of the Hydrological Cycle to Global Warming. *Journal of Climate* **19**, 5686–5699 (2006).
5. Helm K. P., Bindoff N. L. & Church J. A. Changes in the global hydrological-cycle inferred from ocean salinity: hydrological cycle and ocean salinity. *Geophys. Res. Lett.* **37**, L18701 (2010).
6. Durack, P. J., Wijffels, S. E. & Matear, R. J. Ocean Salinities Reveal Strong Global Water Cycle Intensification During 1950 to 2000. *Science* **336**, 455–458 (2012).
7. Levang, S. J. & Schmitt, R. W. Centennial Changes of the Global Water Cycle in CMIP5 Models. *Journal of Climate* **28**, 6489–6502 (2015).
8. Lyu, Y., Bindoff, N. L., Mohapatra, S., Rathore, S. & Phillips, H. E. Global Water Cycle Pattern Amplification: Contributing Factors and Mechanisms. *Journal of Geophysical Research: Oceans* **130**, e2024JC022278 (2025).
9. Vinogradova, N. T. & Ponte, R. M. In Search of Fingerprints of the Recent Intensification of the Ocean Water Cycle. *Journal of Climate* **30**, 5513–5528 (2017).
10. Ponte, R. M. & Vinogradova, N. T. An assessment of basic processes controlling mean surface salinity over the global ocean. *Geophysical Research Letters* **43**, 7052–7058 (2016).
11. Liu, X., Köhl, A. & Stammer, D. Dynamical ocean response to projected changes of the global water cycle. *Journal of Geophysical Research: Oceans* **122**, 6512–6532 (2017).

12. Douville, H. & Cheng, L. Asymmetric Sea Surface Salinity Response to Global Warming: "Fresh Gets Fresher but Salty Hesitates". *Geophysical Research Letters* **51**, e2023GL107944 (2024).

13. Yu, L. & Toole, J. M. Subtropical gyre expansion causes Southern Ocean salinification contrary to freshening predictions. *Nat Commun* **17**, 8924 (2026).

14. Sun, Q. *et al.* Sea Surface Salinity Change since 1950: Internal Variability versus Anthropogenic Forcing. *Journal of Climate* **34**, 1305–1319 (2021).

15. Hawkins, E. & Sutton, R. Time of emergence of climate signals. *Geophysical Research Letters* **39**, 2011GL050087 (2012).

16. Schneider, D. P., Maher, N., Dong, Y., Kay, J. E. & Capotondi, A. Observable polar and Atlantic sea surface salinity trends have emerged, while the noisy Indo-Pacific hesitates. *Environ. Res.: Climate* **4**, 045002 (2025).

17. Silvy, Y., Guilyardi, E., Sallée, J.-B. & Durack, P. J. Human-induced changes to the global ocean water masses and their time of emergence. *Nat. Clim. Chang.* **10**, 1030–1036 (2020).

18. Tjiputra, J. F., Negrel, J. & Olsen, A. Early detection of anthropogenic climate change signals in the ocean interior. *Sci Rep* **13**, 3006 (2023).

19. Eyring, V. *et al.* Overview of the Coupled Model Intercomparison Project Phase 6 (CMIP6) experimental design and organization. *Geosci. Model Dev.* **9**, 1937–1958 (2016).

20. O'Neill, B. C. *et al.* The Scenario Model Intercomparison Project (ScenarioMIP) for CMIP6. *Geosci. Model Dev.* **9**, 3461–3482 (2016).

21. Herger, N., Sanderson, B. M. & Knutti, R. Improved pattern scaling approaches for the use in climate impact studies. *Geophysical Research Letters* **42**, 3486–3494 (2015).

22. Lyu, K., Zhang, X., Church, J. A., Slangen, A. B. A. & Hu, J. Time of emergence for regional sea-level change. *Nature Clim Change* **4**, 1006–1010 (2014).

23. Schlunegger, S. *et al.* Time of Emergence and Large Ensemble Intercomparison for Ocean Biogeochemical Trends. *Global Biogeochemical Cycles* **34**, e2019GB006453 (2020).

24. Lyu, K., Zhang, X., Church, J. A. & Hu, J. Quantifying internally generated and externally forced climate signals at regional scales in CMIP5 models. *Geophysical Research Letters* **42**, 9394–9403 (2015).

25. Schleussner, C.-F. *et al.* Science and policy characteristics of the Paris Agreement temperature goal. *Nature Clim Change* **6**, 827–835 (2016).

26. Tebaldi, C. & Arblaster, J. M. Pattern scaling: Its strengths and limitations, and an update on the latest model simulations. *Climatic Change* **122**, 459–471 (2014).

27. Skliris, N., Zika, J. D., Nurser, G., Josey, S. A. & Marsh, R. Global water cycle amplifying at less than the Clausius-Clapeyron rate. *Sci Rep* **6**, 38752 (2016).

28. Yu, L. Ocean salinity across space-time scales: from water cycle indicator to dynamical driver. *Ocean Sci.* **22**, 1651–1679 (2026).

29. Lu, J., Vecchi, G. A. & Reichler, T. Expansion of the Hadley cell under global warming. *Geophys. Res. Lett.* **34**, L06805 (2007).

30. Staten, P. W., Lu, J., Grise, K. M., Davis, S. M. & Birner, T. Re-examining tropical expansion. *Nature Clim Change* **8**, 768–775 (2018).

31. Zhou, W., Xie, S.-P. & Yang, D. Enhanced equatorial warming causes deep-tropical contraction and subtropical monsoon shift. *Nat. Clim. Chang.* **9**, 834–839 (2019).

32. Stott, P. A., Sutton, R. T. & Smith, D. M. Detection and attribution of Atlantic salinity changes. *Geophysical Research Letters* **35**, 2008GL035874 (2008).

33. Pierce, D. W., Gleckler, P. J., Barnett, T. P., Santer, B. D. & Durack, P. J. The fingerprint of human-induced changes in the ocean's salinity and temperature fields. *Geophysical Research Letters* **39**, 2012GL053389 (2012).

34. Terray, L. *et al.* Near-Surface Salinity as Nature's Rain Gauge to Detect Human Influence on the Tropical Water Cycle. *Journal of Climate* **25**, 958–977 (2012).

35. Swart, N. C., Gille, S. T., Fyfe, J. C. & Gillett, N. P. Recent Southern Ocean warming and freshening driven by greenhouse gas emissions and ozone depletion. *Nature Geosci* **11**, 836–841 (2018).

36. Seneviratne, S. I., Donat, M. G., Pitman, A. J., Knutti, R. & Wilby, R. L. Allowable CO2 emissions based on regional and impact-related climate targets. *Nature* **529**, 477–483 (2016).

37. James, R., Washington, R., Schleussner, C.-F., Rogelj, J. & Conway, D. Characterizing half-a-degree difference: a review of methods for identifying regional climate responses to global warming targets. *WIREs Climate Change* **8**, e457 (2017).

38. Durack, P. J. & Wijffels, S. E. Fifty-Year Trends in Global Ocean Salinities and Their Relationship to Broad-Scale Warming. *Journal of Climate* **23**, 4342–4362 (2010).

39. Zika, J. D. *et al.* Improved estimates of water cycle change from ocean salinity: the key role of ocean warming. *Environ. Res. Lett.* **13**, 074036 (2018).

40. Gould, W. J. & Cunningham, S. A. Global-scale patterns of observed sea surface salinity intensified since the 1870s. *Commun Earth Environ* **2**, 76 (2021).

41. Skliris, N. *et al.* Salinity changes in the World Ocean since 1950 in relation to changing surface freshwater fluxes. *Clim Dyn* **43**, 709–736 (2014).

42. Vinogradova, N. T. & Ponte, R. M. Clarifying the link between surface salinity and freshwater fluxes on monthly to interannual time scales. *JGR Oceans* **118**, 3190–3201 (2013).

43. Ge, K. *et al.* Surface Salinity Changes of the Tropical and Subtropical Oceans Since 1970 and Their Relationship With Surface Freshwater Fluxes. *Journal of Geophysical Research: Oceans* **128**, e2023JC020207 (2023).

44. Pang, S., Vialard, J., Lengaigne, M. & Wang, X. Tropical Salinity Contrast Strengthening in CMIP6: Inter-Model Diversity and Mechanisms. *Earth's Future* **14**, e2025EF007346 (2026).

45. Iwakiri, T. *et al.* AMOC slowdown amplifies North Atlantic salinity variability to unprecedented levels. *Nat Commun* **17**, 7021 (2026).

46. Lu, Y. *et al.* North Atlantic–Pacific salinity contrast enhanced by wind and ocean warming. *Nat. Clim. Chang.* **14**, 723–731 (2024).

47. Sohail, T., Zika, J. D., Irving, D. B. & Church, J. A. Observed poleward freshwater transport since 1970. *Nature* **602**, 617–622 (2022).

48. Liu, H., Xu, T., Li, D., Nie, X. & Wei, Z. Sea surface salinity extremes over the global ocean. *Environ. Res. Lett.* **18**, 114020 (2023).

49. Malan, N., Roughan, M., Hemming, M. & Ingleton, T. Quantifying coastal freshwater extremes during unprecedented rainfall using long timeseries multi-platform salinity observations. *Nat Commun* **15**, 424 (2024).

50. Good, S. A., Martin, M. J. & Rayner, N. A. EN4: Quality controlled ocean temperature and salinity profiles and monthly objective analyses with uncertainty estimates. *JGR Oceans* **118**, 6704–6716 (2013).

51. Cheng, L. *et al.* Improved Estimates of Changes in Upper Ocean Salinity and the Hydrological Cycle. *Journal of Climate* **33**, 10357–10381 (2020).

52. Zuo, H., Balmaseda, M. A., Tietsche, S., Mogensen, K. & Mayer, M. The ECMWF operational ensemble reanalysis–analysis system for ocean and sea ice: a description of the system and assessment. *Ocean Sci.* **15**, 779–808 (2019).

53. Hersbach, H. *et al.* The ERA5 global reanalysis. *Q.J.R. Meteorol. Soc.* **146**, 1999–2049 (2020).

54. Giorgi, F. & Bi, X. Time of emergence (TOE) of GHG-forced precipitation change hot-spots. *Geophysical Research Letters* **36**, (2009).

55. De Boyer Montégut, C., Madec, G., Fischer, A. S., Lazar, A. & Iudicone, D. Mixed layer depth over the global ocean: An examination of profile data and a profile-based climatology. *J. Geophys. Res.* **109**, 2004JC002378 (2004).

Supplementary Files

This is a list of supplementary files associated with this preprint. Click to download.

- SupplementaryData.xlsx
- YuxuanlyuNatureGeoscienceSupplementaryInformation.docx